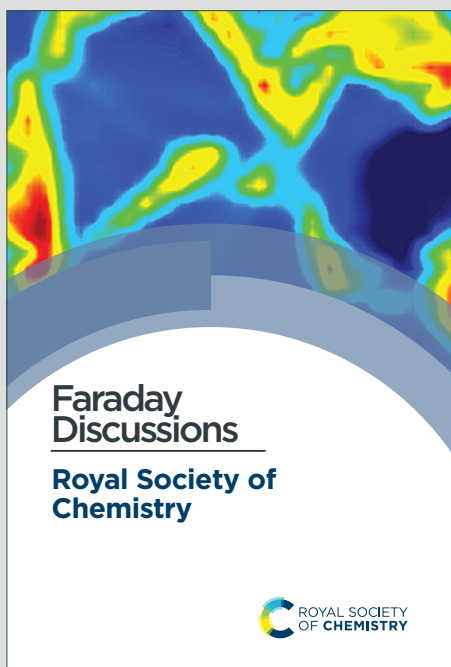


Faraday Discussions

Accepted Manuscript



This is an Accepted Manuscript, which has been through the Royal Society of Chemistry peer review process and has been accepted for publication.

Accepted Manuscripts are published online shortly after acceptance, before technical editing, formatting and proof reading. Using this free service, authors can make their results available to the community, in citable form, before we publish the edited article. We will replace this Accepted Manuscript with the edited and formatted Advance Article as soon as it is available.

You can find more information about Accepted Manuscripts in the [Information for Authors](#).

Please note that technical editing may introduce minor changes to the text and/or graphics, which may alter content. The journal's standard [Terms & Conditions](#) and the [Ethical guidelines](#) still apply. In no event shall the Royal Society of Chemistry be held responsible for any errors or omissions in this Accepted Manuscript or any consequences arising from the use of any information it contains.

This article can be cited before page numbers have been issued, to do this please use: M. Carmiel, Y. Hovav, A. Theodoridis, C. Langhammer and E. Gross, *Faraday Discuss.*, 2026, DOI: 10.1039/D5FD00167F.

Structure-Controlled Sulfur Poisoning and Hydrogen-Induced Regeneration in Single Pd Nanoparticles Probed by Nanospectroscopy

View Article Online
DOI: 10.1039/D5FD00167F

Mazal Kostan-Carmiel¹, Yehonatan Hovav¹, Athanasios Theodoridis², Christoph Langhammer² and Elad Gross¹

1. Institute of Chemistry, and the Center for Nanoscience and Nanotechnology, The Hebrew University, Jerusalem 91904, Israel
2. Department of Physics, Chalmers University of Technology, Gothenburg 412 96, Sweden



Abstract

View Article Online
DOI: 10.1039/D5FD00167F

Structural order and surface crystallinity of palladium nanoparticles (Pd NPs) significantly affect their chemical and mechanical stability, and impact their resistance to poisoning and efficiency in hydrogen (H_2) (de)sorption. This study investigates the impact of sulfuric acid (H_2SO_4) poisoning on pristine and annealed Pd NPs to identify the influence of structure on the density and stability of poisoners. Electron microscopy and diffraction analyses show that annealing transforms initially amorphous, rough, and aggregated particles into spherical and crystalline NPs with better-defined grain boundaries. Nanoscale AFM-IR analysis show that pristine NPs rapidly decompose SO_x upon H_2 exposure, and SO_x is mainly located on the rim of the NP. Annealed NPs maintain stable, localized SO_x signatures across multiple N_2 - H_2 cycles, and only after the second H_2 exposure cycle the SO_x is removed from the central part of the NP. Contact potential difference analysis show the strong affinity of SO_x to the rim of the NP. Together, these results reveal that crystallinity and defect density dictate both the spatial distribution and chemical stability of sulfur species on Pd surfaces. Pristine, defect-rich NPs promote rapid H_2 -induced SO_x reduction and selective desorption from their centers, whereas annealed, crystalline NPs stabilize SO_x more strongly and exhibit delayed desorption. This direct link between structural order, SO_x binding strength, and hydrogen (de)sorption affinity underscores the critical role of nanoscale morphology in controlling poisoning dynamics and highlights nanospectroscopy as a powerful tool for correlating local structure with chemical functionality.



Introduction

View Article Online
DOI: 10.1039/D5FD00167F

Catalytic behavior of metallic nanoparticles (NPs) is influenced by their atomic arrangement, degree of crystallinity, and distribution of structural defects.^{1–3} Grain size, surface roughness, facet orientation, and defect density all contribute to shaping the electronic structure and adsorption energetics of active sites, thereby governing reaction pathways and catalytic efficiency.^{4–9} Structural imperfections provide highly reactive adsorption sites, including disordered atomic domains, vacancies, steps, and grain boundaries. However, these imperfections can also contribute to mechanical deformation, chemical restructuring, and long-term degradation of the material.¹⁰ Therefore, rational design of catalytic materials requires a clear understanding of the interplay between structural order and chemical functionality.^{11–13}

There has been extensive research demonstrating the influence of structure on catalytic performance across a variety of metallic systems. Amorphous or defect-rich materials often exhibit enhanced initial reactivity due to the presence of high density of reactive surface sites, but may suffer from limited stability or irreversible restructuring.^{14,15} In contrast, crystalline NPs with well-defined facets provide more predictable adsorption behavior and improved stability.^{16–19} Small or irregular NPs often exhibit rapid adsorption kinetics, but experience high lattice strain after repeated reaction exposure, while larger or more faceted particles possess greater mechanical stability.^{20,21} It can be therefore deduced that crystallinity, morphology, and defect density have a crucial impact on the catalytic performance and stability of materials.

Catalyst stability is strongly affected by the susceptibility to surface poisoning. Molecules such as CO, NO_x, H₂O, and sulfur-oxide species (SO_x) can deactivate surface sites, due to strong interaction with the metal surface, preventing reactant adsorption and its activation.^{10,22–24} The poisoning mechanism is highly sensitive to the surface structure. Surfaces with high density of adsorption sites can facilitate strong, sometimes irreversible binding of poisoning species.^{25,26} Consequently, the role and reversibility of catalyst poisoning depend on both the chemical nature of the poisoner and the structural characteristics of the active surface.

Pd NPs are ideal materials for studying structure-function relationships due to their exceptional ability to dissociate and absorb hydrogen. Hydrogen uptake in Pd induces a reversible phase transition accompanied by lattice expansion, making Pd a powerful system for hydrogen storage, catalysis, and sensing.^{9,22,27–30} However, the reversibility and kinetics of phase transition depend strongly on structural and morphological characteristics of Pd NPs,



including size, crystallinity, and surface defect density. Amorphous domains, rough surfaces, and high density of surface defects are common features in pristine Pd NPs, which enhance their hydrogen sorption rates, but also induce irreversible lattice strain upon repeated cycling.^{30,31} Alternatively, thermal annealing can be used to transform amorphous Pd NPs into polycrystalline nanostructures that are characterized with smooth surfaces and lower defect density. This structural change does not only enhance the particle uniformity but also leads to more predictable and reversible phase transitions during hydrogen (de)sorption cycling.^{30,32,33} Therefore, structural order is directly related to mechanical robustness, phase-transition reversibility, and hydrogen reactivity in Pd-based nanomaterials.^{34–37}

Pd surfaces are highly vulnerable to poisoning, and specifically to sulfur poisoning.^{9,38,39} SO_x species bind strongly to Pd, blocking H₂ dissociation sites and significantly reducing their catalytic activity.⁹ Defect-rich, pristine Pd NPs provide a significant number of high-energy adsorption sites, which result in rapid SO_x accumulation and accelerated deactivation. Annealed Pd NPs, on the other hand, exhibits a lower defect density and well-defined crystallographic facets, resulting in a higher resistance to sulfur adsorption as well as a higher recovery following H₂ exposure.⁴⁰

Due to their structural complexity, which induces both inter- and intra-particle variances, a comprehensive understanding of structure-reactivity correlations in Pd NPs requires an in-depth nano-scale analysis.^{41–43} Such analysis will enable spatial mapping of poisoners' distribution and reveal how variations in surface coordination influence the adsorption strength, stability and diffusivity of sulfur-based species. Recent advances in high spatial resolution spectroscopy have enabled nanoscale investigations of catalytic nanoparticles.^{7,8,44–54} In particular, infrared (IR) nanospectroscopy measurements^{55,56} have shown that the types and adsorption geometries of SO_x species vary significantly due to morphological and structural heterogeneity among individual nanoparticles.^{9,39} However, the connection between crystallinity, location-dependent SO_x adsorption (rim vs. center), and the kinetics of H₂-induced SO_x reduction remains insufficiently resolved.

Herein, we combine AFM-IR, KPFM, and electron microscopy to correlate the structural evolution of pristine versus annealed Pd NPs with their sulfur-poisoning behavior. We show that annealing transforms amorphous, highly corrugated particles into crystalline nanostructures with smoother surfaces, which in turn stabilizes SO_x species and delays their H₂-induced desorption. In contrast, pristine NPs exhibit rapid SO_x reduction and selective desorption from their central regions, with preferential retention at defect-rich rim sites.

View Article Online
DOI: 10.1039/D5FD00167F



These insights establish a direct structure-poisoning relationship and highlight how crystallinity governs both SO_x stability and hydrogen (de)sorption dynamics.

View Article Online
DOI: 10.1039/D5FD00167F

Experimental

Nanofabrication of Pd NPs samples. Pd nanodisk arrays were fabricated on 1x1 cm fused silica substrates using Hole-mask Colloidal Lithography (HCL).⁵⁷ The particles had a nominal size of 210 nm (diameter) and 25 nm (height), covering approx. 10% of the total sample area. For the annealed NPs subsequent annealing was performed at 500 °C for 18 h under a flow of 2 vol.% H₂ in Ar.

AFM-IR and KPFM measurements. Atomic force microscopy Infrared (AFM-IR) and Kelvin probe force microscopy (KPFM) measurements were performed at a tapping mode using a nanoIR-3 setup (Anasys, Bruker). AFM-IR setup is equipped with a Bruker Hyperspectral Quantum Cascade Lasers (QCL) laser source (790-1950 cm⁻¹), a gold-coated Si probes with a nominal diameter of ~25 nm, resonance frequencies of 75±15 kHz, and spring constants of 1-7 N m⁻¹. Spectra were acquired with an average integration time of 5 s per spectrum and a spectral resolution of 2 cm⁻¹. For each measurement point, IR spectra were obtained by averaging five consecutive spectra collected at the same location on the nanoparticle. KPFM measurements were performed using a Pt/Ir probes with a nominal diameter of ~25 nm, resonance frequency of 62±14 kHz, and spring constants of 1-6 N m⁻¹. Nano-IR measurements were conducted *in-situ* at room temperature under exposure to varying gas environments (1 atm of N₂ or 1 atm of 100:1 N₂:H₂ for 60 minutes), with humidity values less than 10%.

H₂SO₄ poisoning. Sulfur poisoning of Pd NPs was performed by immersing the sample in a 10 mM aqueous H₂SO₄ solution for 10 min at 25 °C. Following exposure, the sample was dried on a hot plate in air at 100–110 °C for 10 min to remove physisorbed surface residues. The poisoning conditions were selected based on previous studies demonstrating that these conditions preserve the structure of both the Pd nanoparticles and the substrate, while harsher conditions induce structural changes.³⁹

FIB-TEM measurements. Lamella of Pd NPs for Scanning Transmission Electron Microscopy (STEM) imaging was prepared using a Focused-Ion Beam (FIB), (Helios NanoLab 460F1). STEM images were taken using an aberration probe-corrected Themis Z-G3 (Thermo Fisher



Scientific) operated at 300 kV, equipped with an Annular Dark Field Detector (HAADF) for diffraction pattern of single Pd NP.

View Article Online
DOI: 10.1039/D5FD00167F

Results and discussion

Pd NPs were prepared on a Si (100) wafer with a native oxide layer by using Hole-mask Colloidal Lithography nanofabrication. In order to prepare NPs that are characterized with a better-defined structure, the NPs were annealed to 500 °C for 18 h under a flow of 2% v/v H₂ in Ar. The chosen annealing temperature is above the Huttig temperature ($0.3 T_m$, T_m = melting temperature of Pd = 1828 K) of Pd (275 °C) and below the Tammann temperature ($0.5 T_m$, ~650 °C) and thus lead to surface atom diffusion and smoothing without sintering of nanoparticles due to ripening and migration. High-resolution TEM (HR-TEM) imaging show the morphology and structure of the pristine and annealed Pd NPs (Figure 1a-b and e-f, respectively).

characterization was conducted by using FIB to extract a lamella and its analysis by TEM imaging and fast Fourier transform (FFT) analysis of the diffraction pattern of the pristine and annealed NPs (Figure 1c-d and 1g-h, respectively).

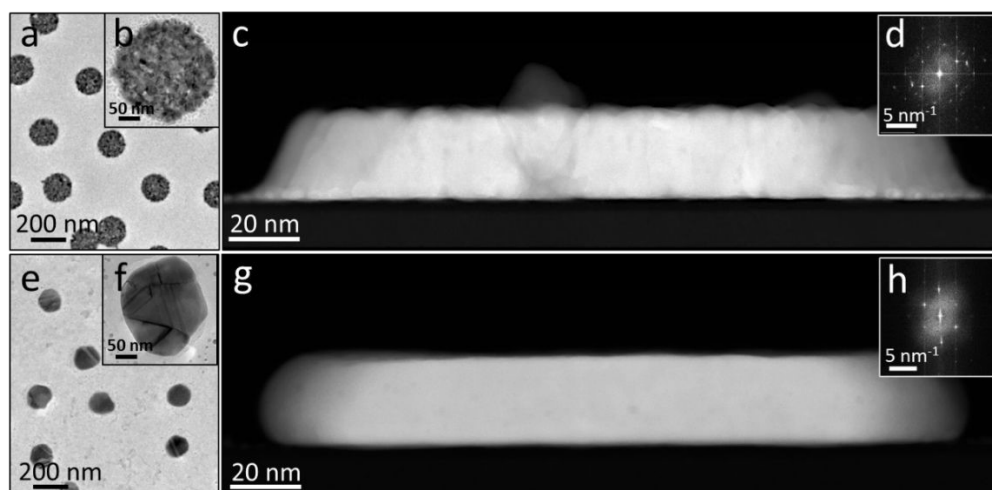


Figure 1. TEM (a and e), HR-TEM (b and f), FIB-TEM cross-sectional images (c and g) and FFT diffraction patterns (d and h) of pristine and annealed Pd NPs, respectively.

Both samples included NPs with a diameter and height of 190 ± 10 and 25 ± 5 nm, respectively. It was also identified that the pristine NPs are characterized with a more corrugated surface, that is constructed of nanoscale aggregates (Figure 1a-b). The annealed NPs showed a more spherical morphology with smoother surfaces, better-defined particle boundaries, and



enhanced crystallinity (Figure 1e-f), which are consistent with thermally driven intra-particle sintering and grain growth.

View Article Online
DOI: 10.1039/D5FD00167F

TEM cross-sections of the pristine NP revealed a largely amorphous structure, as indicated by the diffuse, disordered FFT patterns (figure 1c-d). Conversely, annealed NPs displayed a different morphology, while the TEM cross-sections revealed sharply defined crystalline domains, and the corresponding FFT images exhibited distinct diffraction pattern that is consistent with a well-ordered face-centered cubic (FCC) structure (Figure 1g-h). These results confirm that thermal annealing promotes the transformation of disordered Pd NPs into nanostructures that are more robust, with defined crystalline domains and lower density of grain boundaries.

The pristine and annealed NPs were immersed in H₂SO₄ (10 mM, 25 °C, 10 minutes), followed by heating the dried sample in air (110 °C, 10 minutes) to remove physisorbed residues. Localized IR spectra were acquired from the center of the pristine and annealed NPs (Figure 2a and 2b, respectively). The pristine NP exhibited characteristic IR absorption bands (Figure 2a, blue colored spectrum) at 1100, 1194 and 1228 cm⁻¹. The feature at 1100 cm⁻¹ was assigned to sulfates adsorbed with 3-fold geometry on metallic sites (Pd⁰) of Pd(111) facets, while to peak at 1194 cm⁻¹ is attributed to sulfates adsorbed with 3-fold geometry with the C_{3v} symmetry on electron-deficient Pd_x⁺ sites.⁵⁸ The peak at 1228 cm⁻¹ is attributed to SO₂ species.⁵⁹ The peak at 1451 cm⁻¹ was assigned to 2-fold or 3-fold sulfates adsorbed on oxidized Pd sites (i.e., Pd_x⁺). The annealed NP (Figure 2b, blue colored spectrum) showed signals at 1048 and 1095 cm⁻¹, correlated to symmetric and asymmetric S-O stretching of sulfate, respectively, while the minor signal at 1264 cm⁻¹ was correlated to SO₂. The detection of a broad absorbance band at 1000-1150 cm⁻¹ with a split to two peaks is correlated to sulfate adsorption at a bidentate adsorption mode with a C_{2v} symmetry.⁵⁸



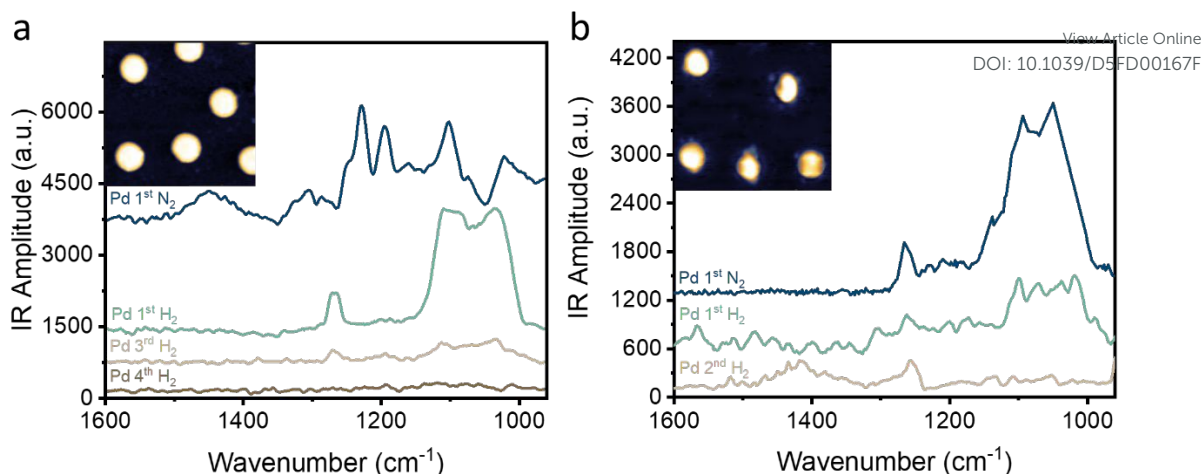


Figure 2. IR nanospectroscopy measurements acquired on the center of pristine (a) and annealed (b) NPs after their exposure to H_2SO_4 . IR spectra were acquired following exposure to cycles of N_2 and H_2 .

After exposure to H_2 the IR signal of the pristine sample (Figure 4a, green-colored spectrum) was similar to that of the annealed sample, with two dominant peaks at 1035 and 1108 cm^{-1} and a smaller peak at 1267 cm^{-1} . The disappearance of the peaks at 1228 cm^{-1} , coupled with the presence of a new peak at 1267 cm^{-1} , was assigned to structural changes that modified the adsorption geometry.⁶⁰ Consecutive H_2 - N_2 cycles led to an overall decrease in the SO_x signal and after 3 cycles only a minor signature was detected on the pristine NP. No signal was detected on the central part of the NPs after the 4th cycle, indicative of SO_x desorption from the center of the NP (Figure 4a, brown-colored spectrum).

Exposure to H_2 reduced the vibrational signals on the annealed NP to about $1/3$ of their initial amplitude. After exposure to a second cycle of H_2 , the IR signals at the 1000 - 1100 cm^{-1} range were not detected. The peak at 1264 cm^{-1} was attributed to SO_2 species.⁵⁹ The peak at 1420 cm^{-1} was assigned to 2-fold or 3-fold sulfates adsorbed on oxidized Pd sites (i.e., Pd_x^+). It can be concluded that exposure to H_2SO_4 led to the formation of different surface chemistry on the pristine and annealed NPs.

Quantitative analysis of surface roughness was performed based on AFM measurements (Figure 3). The pristine NPs exhibited an average surface roughness of 3.12 ± 0.17 nm, which increased to 3.40 ± 0.10 nm after exposure to H_2SO_4 (Figure 3, black colored curves). Following two cycles of exposure to N_2 and H_2 the roughness value decreased to 3.25 ± 0.08 nm. The annealed Pd NPs displayed a smoother surface, with an overall roughness of 1.92 ± 0.29 nm before exposure to H_2SO_4 , which decreased to 1.24 ± 0.20 nm after poisoning. Following two cycles of exposure to N_2 and H_2 the roughness values of both the pristine and annealed



samples showed a moderate decrease. It was previously demonstrated by us that due to their high structural similarity of the nanoparticles, analysis of five nanoparticles provides statistically meaningful values that are representative of the behavior of the nanoparticle array.⁹

View Article Online
DOI: 10.1039/D5FD00167F

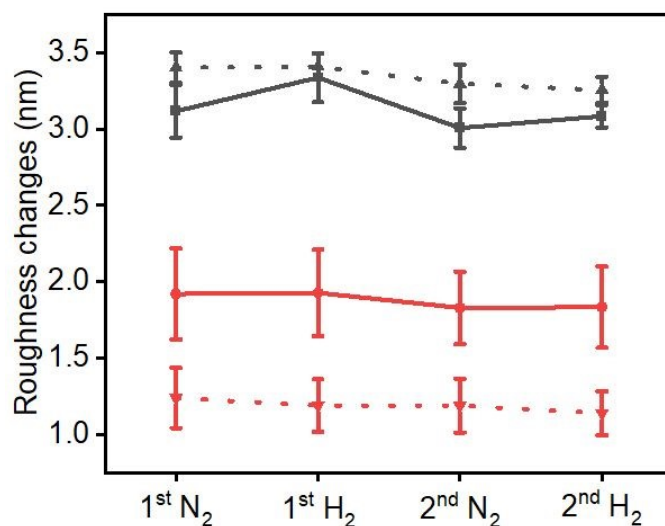


Figure 3. Average surface roughness of pristine (black) and annealed (red) NPs following sequential N₂-H₂ cycles, shown before (solid lines) and after H₂SO₄ poisoning (dotted lines). Error bars represent the standard deviation across the analyzed particles, based on average of five NPs.

Nanoscale IR mapping were performed to correlate the structural properties with the distribution and stability of poisoners. Nanoscale AFM-IR mapping was performed at 1108 cm⁻¹, correlated to the asymmetric S-O vibration of SO₄²⁻ (Figure 4a). Quantitative analysis of the variance in the IR amplitude on single NPs was performed by dividing the NP surface to concentric rings and averaging the IR signal across the ring (Figure 4b). The averaged IR signal of each ring was then plotted as function of the radial distance of the ring from the center of the NP to provide a quantitative analysis of the IR signal amplitude on different sites of the NP (Figure 4c).



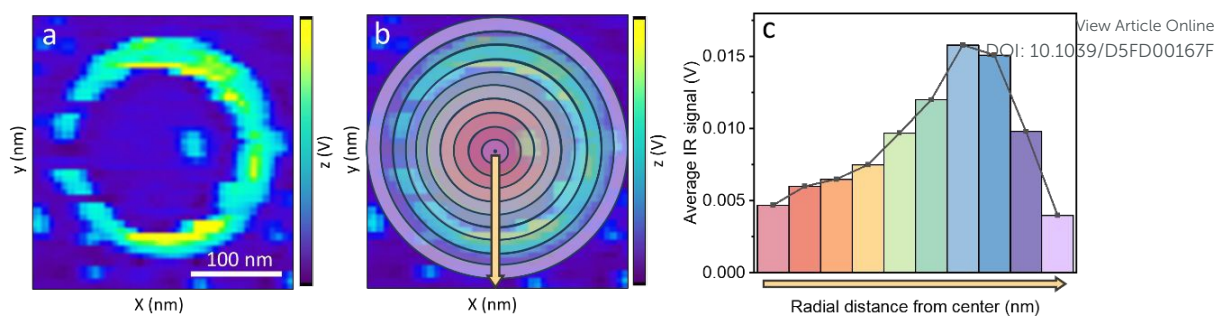


Figure 4. Quantitative analysis of AFM-IR mapping. (a) AFM-IR mapping of pristine NP following H_2SO_4 poisoning was recorded at 1108 cm^{-1} . (b) Quantitative analysis of the IR signal across the NP surface was performed by dividing the NP into concentric rings, each with a fixed width of ~ 4.5 pixels ($\approx 3\text{ nm}$), and calculating the averaged IR signal within each ring. Ten rings are shown as an example in (b). The averaged signal of each ring was then plotted as a function of its distance from the nanoparticle's center of mass (c). The yellow arrow indicates the radial distance measured from the particle's center of mass.

AFM-IR maps were recorded for the pristine and annealed NPs (Figure 5a and 5c, respectively) after exposure to H_2SO_4 and following consecutive N_2 and H_2 cycles. Quantitative analysis of the IR signal was performed for two pristine and annealed NPs (Figure 5b and 5d, respectively), in a similar approach to the one described in Figure 4. The pristine NPs showed an AFM-IR signal that covered the NPs, indicating that the NPs are coated with SO_x molecules (Figure 5a). Analysis of the AFM-IR maps showed a similar signal on the central part of the NP with a continuous decrease in the IR signal toward the edge of the NPs (Figure 5b, black-colored curve). Following exposure to H_2 , the IR signal in the central part of the pristine NPs decreased and a ring of IR signal was detected on the outer rim of the NP (Figure 5a). This was also validated by analysis of the IR signals (red-colored curve, Figure 5b). A second exposure cycle to N_2 (blue-colored curve, Figure 5b) and to H_2 (green-colored curve, Figure 5b) led to sharpening of the IR signal toward the rim of the NP. These results show the selective desorption of SO_x from the central part of the NP following exposure to H_2 .



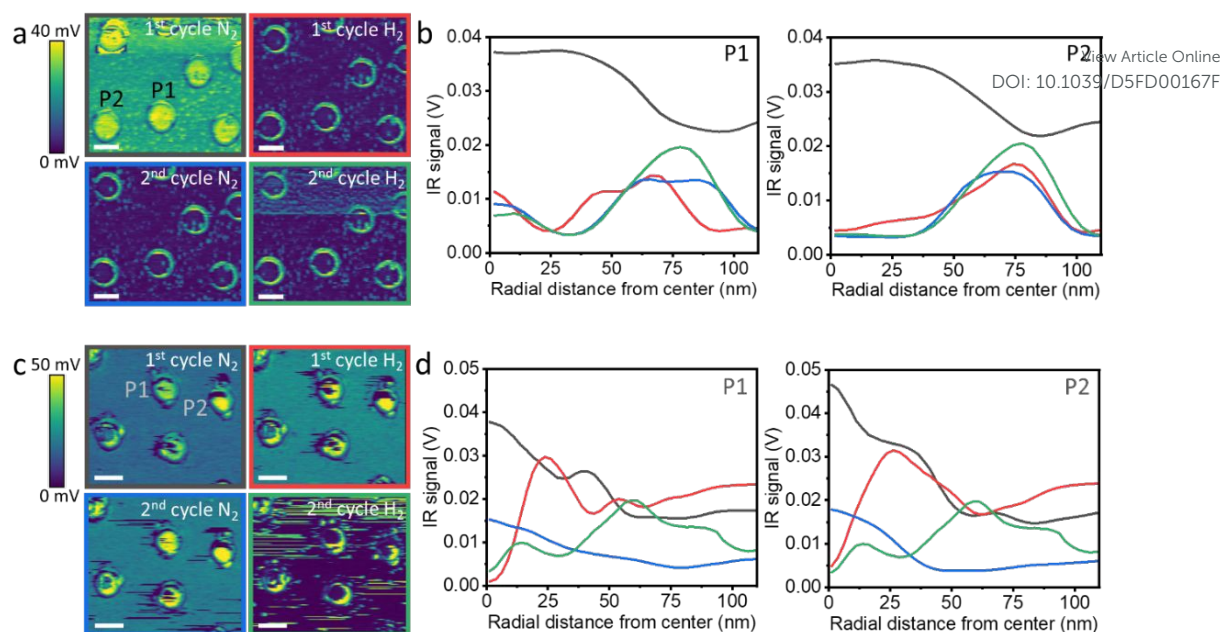


Figure 5. AFM-IR mapping at 1108 cm^{-1} of pristine (a) and annealed (c) Pd NPs after exposure to H_2SO_4 and following consecutive N_2 and H_2 cycles. The surfaces of two NPs (labeled P1 and P2 in panels a and c) were divided into concentric rings, and the averaged IR signal of each ring was plotted as a function of the radial distance from the particle center. The radial IR signal analysis of the pristine and annealed NPs are shown in panels b and d, respectively. Data in b and d are shown after the first exposure to N_2 and H_2 (black and red traces, respectively) and after the second exposure to N_2 and H_2 (blue and green traces, respectively). The scale bar represents 200 nm.

A different pattern was detected for the annealed NP. AFM-IR imaging probed the selective desorption of SO_x species only after the second H_2 cycle (Figure 5c). Quantitative analysis of the IR signal showed that prior to exposure to H_2 , the IR signal reached its maximum at the center of the NP and moderately decreased toward the edges of the NP (black colored curve, Figure 5d). Following H_2 exposure, the maximum IR signal shifted from the centre toward the rim of the NP (red colored curve, Figure 5d) and this shift further increased after the second H_2 exposure (green colored curve, Figure 5d).

These observations are consistent with the analysis of surface roughness (Figure 3). Pristine NPs exhibit higher surface corrugation values, and noticeable changes in surface roughness were measured following exposure to H_2 , indicating a dynamic and adaptable surface structure. Due to enhanced atomic mobility, SO_x diffusion and desorption occurred during H_2 exposure, presumably due to dissociation of H_2 that enabled the following reduction and desorption of SO_x species. The annealed NPs exhibit smaller and more consistent roughness variations, indicating that the surface is structurally more stable. In addition, it is expected



that H₂ dissociation will have higher kinetic barriers on a surface with lower density of surface defects. Thus, the rate of SO_x reduction, followed by desorption, is expected to be slower on the annealed NPs. For both the pristine and annealed NPs there is higher stability of SO_x on the edge of the NP, correlated with higher density of surface defects on these sites.

KPFM measurements were performed to probe the changes in contact potential difference (CPD), which reflects the difference in work function between the tip and sample (Figure 6). As the transformation from metal to metal-hydride is expected to influence the work function value, KPFM measurements can shed light on the hydrogenation on the particle's top layers on the impact of surface poisoning on hydrogen (de)sorption kinetics.

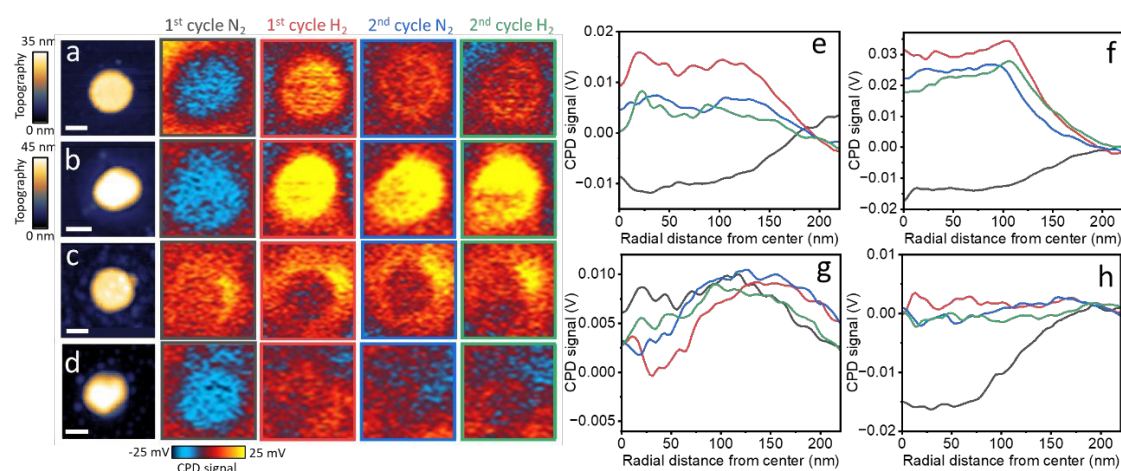


Figure 6. AFM topography and KPFM of the pristine (a and c) and annealed (b and d) Pd NPs. Measurements were performed before (a and b, respectively) and after H₂SO₄ poisoning (c and d, respectively), following consecutive exposure to N₂ and H₂. The radial CPD signal analysis for the pristine (e and f) and annealed (g and h) NPs before (e and g) and after (f and h) H₂SO₄ poisoning are shown. CPD analysis is shown after the first exposure to N₂ and H₂ (black and red traces, respectively) and after the second exposure to N₂ and H₂ (blue and green traces, respectively). Scale bar represents 200 nm.

AFM topography and CPD mapping was performed for pristine and annealed NPs before (Figure 6a and 6b, respectively) and after (Figure 6c and 6d, respectively) exposure to H₂SO₄ following alternating cycles of N₂ and H₂. CPD measurements show noticeable differences in the CPD values of the pristine NP following the initial exposure to H₂ (Figure 6a). Quantitative analysis of the CPD signal show that the CPD values at the center of the NP increased by ~25 mV after the initial exposure to H₂ (red colored curve, Figure 6e). In the second N₂ and H₂ exposure cycle relatively minor changes were probed in CPD values. Interestingly, the CPD values at the rim of the NP showed higher signal than the center of the NP, demonstrating the high reactivity and affinity of hydrogen to these sites.



The annealed NP displayed noticeable changes in CPD values of up to 40 mV following H₂ exposure (Figure 6b and red colored curve in Figure 6f), indicative of enhanced hydrogen sorption affinity, correlated to improved crystallinity that led to higher diffusivity of hydrogen in the NP. Local enhancement in CPD values was measured at the rim of the NP, correlated to higher density of surface defects on these sites. For both the pristine and annealed NPs, smaller changes were probed in the second N₂-H₂ exposure cycle, in comparison to the first cycle, attributed to slower kinetic in hydrogen desorption from the top layers of the NPs.

Following H₂SO₄ poisoning, the CPD values of the pristine NP showed noticeable differences of up to 10 mV between the rim and the center of the NP (Figure 6c and red colored curve in Figure 6g). The non-homogeneous CPD signal along the NP's rim reflects the structural variance and heterogeneity in SO_x adsorption pattern that changed the hydrogen sorption affinity. Nevertheless, although the adsorption of SO_x species is located at rim sites (Figure 4a), the magnitude of response to H₂ exposure is much smaller compare to the non-poisoned pristine NPs (Figure 6a). These results show the dominant effect of sulfate adsorption at rim sites on the overall hydrogen sorption affinity. In contrast, the annealed sample that was poisoned by SO_x showed a more homogeneous CPD distribution after the first H₂ exposure (Figure 6d and 6h).

These trends are consistent with the AFM-IR mapping results (Figure 5a). After the first H₂ exposure, the pristine NPs displayed IR signature on the rim of the NP and this IR signature was identified as well in the CPD analysis. The annealed Pd NPs maintained stable IR signatures across the surface until the second H₂ exposure (Figure 5b), which promoted SO_x sorption. Therefore, the CPD values do not show the rim signal that was detected for the pristine NP and show a moderate response to the changes from N₂ to H₂ environments due to surface poisoning of the NP.

Conclusions

This work demonstrates how the structure of Pd NPs governs their chemical reactivity, hydrogen (de)sorption affinity, and susceptibility to sulfur poisoning. Pristine Pd NPs, characterized by rough, defect-rich surfaces and largely amorphous interiors, exhibit rapid adsorption and reduction of SO_x species during H₂ exposure. In contrast, thermal annealing produces crystalline Pd nanostructures with reduced defect densities, leading to more spatially and chemically uniform SO_x adsorption.



Nanoscale AFM-IR mapping reveals that SO_x species distribute and evolve differently on pristine and annealed NPs. Pristine particles show rapid depletion of SO_x from their centers and selective retention at their more defective rims. Annealed NPs exhibit more stable SO_x signatures, with desorption occurring only after two cycles of hydrogen exposure. These trends correlate with AFM-derived surface roughness measurements and KPFM results, both of which confirm the more pronounced effect of poisoning on the annealed NPs, correlated to the lower density of surface defects, which limits the dissociative adsorption of H₂, followed by reduction and desorption of the adsorbed SO_x species.

These results establish a direct link between nanoscale crystallinity, defect density, and sulfur poisoning dynamics in Pd NPs. Annealed NPs are characterized with structural robustness, that induces stronger sulfur adsorption sites, and quenches the hydrogen sorption affinity. In contrast, pristine NPs are characterized with high density of surface defects, leading to weaker SO_x adsorption sites and improved hydrogen (de)sorption affinity, in comparison to the pristine NPs. These nanospectroscopic insights underscores the importance of structural control in designing durable Pd-based catalysts and hydrogen-responsive sensors, and highlights nanoscale spectroscopy as a powerful tool for correlating local structure with chemical functionality.

Acknowledgements

This research was supported by the Swedish Foundation for Strategic Research (SSF) and Israel's Ministry of Innovation, Science, and Technology (MOST), grant no. 4250, and received funding from the Swedish Foundation for Strategic Research project SIP21-0032 and the Competence Centre TechForH2 (AT, CL). The Competence Centre TechForH2 is hosted by Chalmers University of Technology and is financially supported by the Swedish Energy Agency (P2021-90268) and the member companies Volvo, Scania, Siemens Energy, GKN Aerospace, PowerCell, Oxeon, RISE, Stena Rederier AB, Johnson Matthey, and Insplorion. Part of this work was carried out at the Chalmers MC2 cleanroom facility (μFab)

References

- (1) Hammer, B.; Nørskov, J. K. Theoretical Surface Science and Catalysis-Calculations and Concepts. *Advances in Catalysis*. **2000**, *45*, 71-129. [https://doi.org/10.1016/S0360-0564\(02\)45013-4](https://doi.org/10.1016/S0360-0564(02)45013-4).
- (2) Freund, H. J.; Pacchioni, G. Oxide Ultra-Thin Films on Metals: New Materials for the Design of Supported Metal Catalysts. *Chem Soc Rev* **2008**, *37* (10), 2224–2242. <https://doi.org/10.1039/b718768h>.

View Article Online

DOI: 10.1039/D5FD00167F



- (3) Somorjai, G. A.; Li, Y. Introduction to Surface Chemistry and Catalysis, 2nd ed.; Wiley, **2010**.
View Article Online
DOI: 10.1039/D5FD00167F
- (4) Nilius, N.; Freund, H. J. Activating Nonreducible Oxides via Doping. *Acc Chem Res* **2015**, *48* (5), 1532–1539. <https://doi.org/10.1021/acs.accounts.5b00018>.
- (5) L. Vattuone, L. Savio, M. Rocca. Influence of Defects on Adsorption Model Studies With Stepped Surfaces. *Encyclopedia of Interfacial Chemistry*. **2018**, 38-165. <https://doi.org/10.1016/B978-0-12-409547-2.11461-1>.
- (6) Carmiel-Kostan, M.; Nijem, S.; Dery, S.; Horesh, G.; Gross, E. Composition-Reactivity Correlations in Platinum-Cobalt Nanoporous Network as Catalyst for Hydrodeoxygenation of 5-Hydroxymethylfurfural. *J. Phys. Chem. C* **2019**, *123* (50), 30274–30282. <https://doi.org/10.1021/acs.jpcc.9b07453>.
- (7) Rikanati, L.; Shema, H.; Ben-Tzvi, T.; Gross, E. Nanoimaging of Facet-Dependent Adsorption, Diffusion, and Reactivity of Surface Ligands on Au Nanocrystals. *Nano Lett* **2023**, *23* (12), 5437–5444. <https://doi.org/10.1021/acs.nanolett.3c00250>.
- (8) Friedman, B.; Giloni, L.; Gazit, O. M.; Gross, E. Nanoscale Chemical Imaging of Basic Sites Distribution on Catalytically Active Mg–Al Mixed Oxide Particles. *Chemical and Biomedical Imaging* **2025**, *3* (8), 560–568. <https://doi.org/10.1021/cbmi.5c00017>.
- (9) Kostan-Carmiel, M.; Theodoridis, A.; Eisenberg, H. R.; Stein, T.; Langhammer, C.; Gross, E. Nanoscale Analysis of Sulfur Poisoning Effects on Hydrogen Sorption in Single Pd Nanoparticles. *ACS Nano* **2025**, *19* (42), 36969–36981. <https://doi.org/10.1021/acsnano.5c08917>.
- (10) Bartholomew, C. H. Mechanisms of Catalyst Deactivation, *Applied Catalysis A: General*, **2001**, *212* (1-2), 17-60. [https://doi.org/10.1016/S0926-860X\(00\)00843-7](https://doi.org/10.1016/S0926-860X(00)00843-7).
- (11) Coq, B.; Figueras, F. Structure-Activity Relationships in Catalysis by Metals: Some Aspects of Particle Size, Bimetallic and Supports Effects, *Coordination Chemistry Reviews* **1998**, 178-180, 1753-1783. [https://doi.org/10.1016/S0010-8545\(98\)00058-7](https://doi.org/10.1016/S0010-8545(98)00058-7).
- (12) Vogt, C.; Weckhuysen, B. M. The Concept of Active Site in Heterogeneous Catalysis. *Nature Reviews Chemistry*. Nature Research, **2022**, 89–111. <https://doi.org/10.1038/s41570-021-00340-y>.
- (13) Wen, Y.; Wang, F.; Zhu, J.; Wen, Q.; Xia, X.; Wen, J.; Deng, C.; Du, J. H.; Ke, X.; Zhang, Z.; Guan, H.; Nie, L.; Wang, M.; Hou, W.; Li, W.; Tang, W.; Ding, W.; Chen, J.; Peng, L. Revealing the Structure-Activity Relationship of Pt₁/CeO₂ with ¹⁷O Solid-State NMR Spectroscopy and DFT Calculations. *Nat. Commun* **2025**, *16* (1). <https://doi.org/10.1038/s41467-025-58709-2>.
- (14) George, E. P.; Raabe, D.; Ritchie, R. O. High-Entropy Alloys. *Nat. Rev. Mat.* **2019**, *4*, 515–534. <https://doi.org/10.1038/s41578-019-0121-4>.



- (15) Ibáñez, M.; Boehme, S. C.; Buonsanti, R.; De Roo, J.; Milliron, D. J.; Ithurria, S.; Rogach, A. L.; Cabot, A.; Yarema, M.; Cossairt, B. M.; Reiss, P.; Talapin, D. V.; Protesescu, L.; Hens, Z.; Infante, I.; Bodnarchuk, M. I.; Ye, X.; Wang, Y.; Zhang, H.; Lhuillier, E.; Klimov, V. I.; Utzat, H.; Rainò, G.; Kagan, C. R.; Cargnello, M.; Son, J. S.; Kovalenko, M. V. Prospects of Nanoscience with Nanocrystals: 2025 Edition. *ACS Nano* **2025**, *19* (36), 31969–32051. <https://doi.org/10.1021/acsnano.5c07838>. View Article Online
DOI: 10.1039/D5FD00167F
- (16) Narayanan, R.; El-Sayed, M. A. Shape-Dependent Catalytic Activity of Platinum Nanoparticles in Colloidal Solution. *Nano Lett* **2004**, *4* (7), 1343–1348. <https://doi.org/10.1021/nl0495256>.
- (17) Ma, F.; Ma, S. L.; Xu, K. W.; Chu, P. K. Surface Stability of Platinum Nanoparticles Surrounded by High-Index Facets. *Journal of Physical Chemistry C* **2008**, *112* (9), 3247–3251. <https://doi.org/10.1021/jp077324v>.
- (18) Xiao, C.; Lu, B. A.; Xue, P.; Tian, N.; Zhou, Z. Y.; Lin, X.; Lin, W. F.; Sun, S. G. High-Index-Facet- and High-Surface-Energy Nanocrystals of Metals and Metal Oxides as Highly Efficient Catalysts. *Joule*. **2020**, *4* (12), 2562–2598. <https://doi.org/10.1016/j.joule.2020.10.002>.
- (19) Kang, Y.; João, S. M.; Lin, R.; Liu, K.; Zhu, L.; Fu, J.; Cheong, W. C.; Lee, S.; Frank, K.; Nickel, B.; Liu, M.; Lischner, J.; Cortés, E. Effect of Crystal Facets in Plasmonic Catalysis. *Nat Commun* **2024**, *15* (1). <https://doi.org/10.1038/s41467-024-47994-y>.
- (20) Yang, X. F.; Wang, A.; Qiao, B.; Li, J.; Liu, J.; Zhang, T. Single-Atom Catalysts: A New Frontier in Heterogeneous Catalysis. *Acc Chem Res* **2013**, *46* (8), 1740–1748. <https://doi.org/10.1021/ar300361m>.
- (21) Van Bokhoven, J. A.; Vajda, S. Size Selected Clusters and Particles: From Physical Chemistry and Chemical Physics to Catalysis. *Physical Chemistry Chemical Physics* **2014**, *16* (48), 26418–26420. <https://doi.org/10.1039/c4cp90163k>.
- (22) Darmadi, I.; Nugroho, F. A. A.; Langhammer, C. High-Performance Nanostructured Palladium-Based Hydrogen Sensors - Current Limitations and Strategies for Their Mitigation. *ACS Sensors* **2020**, *5* (11), 3306–3327. <https://doi.org/10.1021/acssensors.0c02019>.
- (23) Hayashi, Y.; Yamazaki, H.; Masunishi, K.; Ikehashi, T.; Nakamura, N.; Kojima, A. Effects of Poisoning Gases on and Restoration of PdCuSi Metallic Glass in a Capacitive MEMS Hydrogen Sensor. *Int J Hydrogen Energy* **2020**, *45* (1), 1187–1194. <https://doi.org/10.1016/j.ijhydene.2019.10.245>.
- (24) Zarabi Golkhatmi, S.; Asghar, M. I.; Lund, P. D. A Review on Solid Oxide Fuel Cell Durability: Latest Progress, Mechanisms, and Study Tools. *Renewable and Sustainable Energy Reviews*. **2022**, *161*, 112339. <https://doi.org/10.1016/j.rser.2022.112339>.



- (25) Xu, X.; Zhong, Y.; Wajrak, M.; Bhatelia, T.; Jiang, S. P.; Shao, Z. Grain Boundary Engineering: An Emerging Pathway toward Efficient Electrocatalysis. *InfoMat.* **2024**, *6* (8), e12608. <https://doi.org/10.1002/inf2.12608>. View Article Online
DOI: 10.1039/D5FD00167F
- (26) Shooshtari Gugtapeh, H.; Aghaii, A. H.; Simchi, A. A Critical Review on the Role of Structural Defects in Electrochemical Nitrate Reduction Catalysts: From Mechanisms to Formation Strategies. *J Environ Chem Eng* **2025**, *13* (6), 120221. <https://doi.org/10.1016/J.JECE.2025.120221>.
- (27) Tittl, A.; Mai, P.; Taubert, R.; Dregely, D.; Liu, N.; Giessen, H. Palladium-Based Plasmonic Perfect Absorber in the Visible Wavelength Range and Its Application to Hydrogen Sensing. *Nano Lett* **2011**, *11* (10), 4366–4369. <https://doi.org/10.1021/nl202489g>.
- (28) Wadell, C.; Syrenova, S.; Langhammer, C. Plasmonic Hydrogen Sensing with Nanostructured Metal Hydrides. *ACS Nano* **2014**, *8* (12), 11925–11940. <https://doi.org/10.1021/nn505804f>.
- (29) Griessen, R.; Strohfeldt, N.; Giessen, H. Thermodynamics of the Hybrid Interaction of Hydrogen with Palladium Nanoparticles. *Nat Mater* **2016**, *15* (3), 311–317. <https://doi.org/10.1038/nmat4480>.
- (30) Andersson, C.; Zimmerman, J.; Fritzsche, J.; Rabkin, E.; Langhammer, C. Hydride Formation Pressures and Kinetics in Individual Pd Nanoparticles with Systematically Varied Levels of Plastic Deformation. *Nat Commun* **2025**, *16* (1), 9242. <https://doi.org/10.1038/s41467-025-64311-3>.
- (31) Delmelle, R.; Amin-Ahmadi, B.; Sinnaeve, M.; Idrissi, H.; Pardoën, T.; Schryvers, D.; Proost, J. Effect of Structural Defects on the Hydriding Kinetics of Nanocrystalline Pd Thin Films. *Int J Hydrogen Energy* **2015**, *40* (23), 7335–7347. <https://doi.org/10.1016/J.IJHYDENE.2015.04.017>.
- (32) Alekseeva, S.; Strach, M.; Nilsson, S.; Fritzsche, J.; Zhdanov, V. P.; Langhammer, C. Grain-Growth Mediated Hydrogen Sorption Kinetics and Compensation Effect in Single Pd Nanoparticles. *Nat Commun* **2021**, *12* (1), 5427. <https://doi.org/10.1038/s41467-021-25660-x>.
- (33) Geng, X.; Li, S.; Heo, J.; Peng, Y.; Hu, W.; Liu, Y.; Huang, J.; Ren, Y.; Li, D.; Zhang, L.; Luo, L. Grain-Boundary-Rich Noble Metal Nanoparticle Assemblies: Synthesis, Characterization, and Reactivity. *Adv Funct Mater* **2022**, *32* (34). <https://doi.org/10.1002/adfm.202204169>.
- (34) Johnson, N. J. J.; Lam, B.; MacLeod, B. P.; Sherbo, R. S.; Moreno-Gonzalez, M.; Fork, D. K.; Berlinguette, C. P. Facets and Vertices Regulate Hydrogen Uptake and Release in Palladium Nanocrystals. *Nat Mater* **2019**, *18* (5), 454–458. <https://doi.org/10.1038/s41563-019-0308-5>.



- (35) Tang, J.; Yamamoto, S.; Koitaya, T.; Yoshigoe, A.; Tokunaga, T.; Mukai, K.; Matsuda, I.; Yoshinobu, J. Mass Transport in the PdCu Phase Structures during Hydrogen Adsorption and Absorption Studied by XPS under Hydrogen Atmosphere. *Appl Surf Sci* **2019**, *480*, 419–426. <https://doi.org/10.1016/J.APSUSC.2019.02.180>. View Article Online
DOI: 10.1039/D5FD00167F
- (36) Ai, B.; Sun, Y.; Zhao, Y. Plasmonic Hydrogen Sensors. *Small* **2022**, *18* (25), 2107882. <https://doi.org/10.1002/smll.202107882>.
- (37) Su, Z.; Zhang, C.; Zhang, X.; Chen, W.; Zhang, X.; Wang, S.; Yang, Y.; Wang, Z. Probe of Nanocatalysts In-Action by Ambient Pressure Photoelectron Spectroscopy. *Nano Research* **2025**, *18* (9), 94907709. <https://doi.org/10.26599/NR.2025.94907709>.
- (38) Mathieu, Y.; Tzanis, L.; Soulard, M.; Patarin, J.; Vierling, M.; Molière, M. Adsorption of SO_x by Oxide Materials: A Review. *Fuel Processing Technology* **2013**, *114*, 81–100. <https://doi.org/10.1016/J.FUPROC.2013.03.019>.
- (39) Say, Z.; Kaya, M.; Kaderoğlu, Ç.; Koçak, Y.; Ercan, K. E.; Sika-Nartey, A. T.; Jalal, A.; Turk, A. A.; Langhammer, C.; Jahangirzadeh Varjovi, M.; Durgun, E.; Ozensoy, E. Unraveling Molecular Fingerprints of Catalytic Sulfur Poisoning at the Nanometer Scale with Near-Field Infrared Spectroscopy. *J Am Chem Soc* **2022**, *144* (19), 8848–8860. <https://doi.org/10.1021/jacs.2c03088>.
- (40) Sun, X.; Li, J.; Fan, J.; Fan, J.; Deng, Q.; Xu, M.; Huang, H.; Wu, J.; Ye, D. Study on Sulfur-Resistant Pd-Based Catalysts for High-Efficiency Oxidation of VOCs. *J Hazard Mater* **2025**, *491*, 137958. <https://doi.org/10.1016/J.JHAZMAT.2025.137958>.
- (41) Xu, W.; Kong, J. S.; Yeh, Y.-T. E.; Chen, P. Single-Molecule Nanocatalysis Reveals Heterogeneous Reaction Pathways and Catalytic Dynamics. *Nat Mater* **2008**, *7* (12), 992–996. <https://doi.org/10.1038/nmat2319>.
- (42) Choi, J. I. J.; Kim, T.-S.; Kim, D.; Lee, S. W.; Park, J. Y. Operando Surface Characterization on Catalytic and Energy Materials from Single Crystals to Nanoparticles. *ACS Nano* **2020**, *14* (12), 16392–16413. <https://doi.org/10.1021/acsnano.0c07549>.
- (43) Groot, I. M. N. Investigation of Active Catalysts at Work. *Acc Chem Res* **2021**, *54* (23), 4334–4341. <https://doi.org/10.1021/acs.accounts.1c00429>.
- (44) Busch, O. M.; Brijoux, W.; Thomson, S.; Schüth, F. Spatially Resolving Infrared Spectroscopy for Parallelized Characterization of Acid Sites of Catalysts via Pyridine Sorption: Possibilities and Limitations. *J Catal* **2004**, *222* (1), 174–179. <https://doi.org/10.1016/J.JCAT.2003.11.002>.
- (45) Roeffaers, M. B. J.; De Cremer, G.; Libeert, J.; Ameloot, R.; Dedecker, P.; Bons, A. J.; Bückins, M.; Martens, J. A.; Sels, B. F.; De Vos, D. E.; Hofkens, J. Super-Resolution Reactivity Mapping of Nanostructured Catalyst Particles. *Angewandte Chemie - International Edition* **2009**, *48* (49), 9285–9289. <https://doi.org/10.1002/anie.200904944>.



- (46) Karreman, M. A.; Buurmans, I. L. C.; Geus, J. W.; Agronskaia, A. V.; Ruiz-Martínez, J.; Gerritsen, H. C.; Weckhuysen, B. M. Integrated Laser and Electron Microscopy Correlates Structure of Fluid Catalytic Cracking Particles to Brønsted Acidity. *Angewandte Chemie - International Edition* **2012**, *51* (6), 1428–1431. <https://doi.org/10.1002/anie.201106651>. View Article Online
DOI: 10.1039/D5FD00167F
- (47) Ruiz-Martínez, J.; Beale, A. M.; Deka, U.; O'Brien, M. G.; Quinn, P. D.; Mosselmans, J. F. W.; Weckhuysen, B. M. Correlating Metal Poisoning with Zeolite Deactivation in an Individual Catalyst Particle by Chemical and Phase-Sensitive X-Ray Microscopy. *Angewandte Chemie - International Edition* **2013**, *52* (23), 5983–5987. <https://doi.org/10.1002/anie.201210030>.
- (48) Wu, C.-Y.; Wolf, W. J.; Levartovsky, Y.; Bechtel, H. A.; Martin, M. C.; Toste, F. D.; Gross, E. High-Spatial-Resolution Mapping of Catalytic Reactions on Single Particles. *Nature* **2017**, *541* (7638), 511–515. <https://doi.org/10.1038/nature20795>.
- (49) Dery, S.; Kim, S.; Haddad, D.; Cossaro, A.; Verdini, A.; Floreano, L.; Toste, F. D.; Gross, E. Identifying Site-Dependent Reactivity in Oxidation Reactions on Single Pt Particles. *Chem Sci* **2018**, *9* (31), 6523–6531. <https://doi.org/10.1039/C8SC01956H>.
- (50) Mao, X.; Liu, C.; Hesari, M.; Zou, N.; Chen, P. Super-Resolution Imaging of Non-Fluorescent Reactions via Competition. *Nat Chem* **2019**, *11* (8), 687–694. <https://doi.org/10.1038/s41557-019-0288-8>.
- (51) Li, Z.; Kurouski, D. Plasmon-Driven Chemistry on Mono- and Bimetallic Nanostructures. *Acc Chem Res* **2021**, *54* (10), 2477–2487. <https://doi.org/10.1021/acs.accounts.1c00093>.
- (52) Dery, S.; Mehlman, H.; Hale, L.; Carmiel-Kostan, M.; Yemini, R.; Ben-Tzvi, T.; Noked, M.; Toste, F. D.; Gross, E. Site-Independent Hydrogenation Reactions on Oxide-Supported Au Nanoparticles Facilitated by Intraparticle Hydrogen Atom Diffusion. *ACS Catal* **2021**, *11* (15), 9875–9884. <https://doi.org/10.1021/acscatal.1c01987>.
- (53) Rikanati, L.; Dery, S.; Gross, E. AFM-IR and s-SNOM-IR Measurements of Chemically Addressable Monolayers on Au Nanoparticles. *J Chem Phys* **2021**, *155* (20), 204704. <https://doi.org/10.1063/5.0072079>.
- (54) Dery, S.; Friedman, B.; Shema, H.; Gross, E. Mechanistic Insights Gained by High Spatial Resolution Reactivity Mapping of Homogeneous and Heterogeneous (Electro)Catalysts. *Chem Rev* **2023**, *123* (9), 6003–6038. <https://doi.org/10.1021/acs.chemrev.2c00867>.
- (55) Dazzi, A.; Prater, C. B. AFM-IR: Technology and Applications in Nanoscale Infrared Spectroscopy and Chemical Imaging. *Chem Rev* **2017**, *117* (7), 5146–5173. <https://doi.org/10.1021/acs.chemrev.6b00448>.



- (56) Kurouski, D.; Dazzi, A.; Zenobi, R.; Centrone, A. Infrared and Raman Chemical Imaging and Spectroscopy at the Nanoscale. *Chem Soc Rev* **2020**, *49* (11), 3315–3347. View Article Online
DOI: 10.1039/D5FD00167F
<https://doi.org/10.1039/C8CS00916C>.
- (57) Fredriksson, H.; Alaverdyan, Y.; Dmitriev, A.; Langhammer, C.; Sutherland, D. S.; Zäch, M.; Kasemo, B. Hole–Mask Colloidal Lithography. *Advanced Materials* **2007**, *19* (23), 4297–4302. <https://doi.org/https://doi.org/10.1002/adma.200700680>.
- (58) Hoshi, N.; Kuroda, M.; Ogawa, T.; Koga, O.; Hori, Y. Infrared Reflection Absorption Spectroscopy of the Sulfuric Acid Anion Adsorbed on Pd(S)–[n(111) × (111)] Electrodes. *Langmuir* **2004**, *20* (12), 5066–5070. <https://doi.org/10.1021/la036149g>.
- (59) Wilburn, M. S.; Epling, W. S. Formation and Decomposition of Sulfite and Sulfate Species on Pt/Pd Catalysts: An SO₂ Oxidation and Sulfur Exposure Study. *ACS Catal* **2019**, *9* (1), 640–648. <https://doi.org/10.1021/acscatal.8b03529>.
- (60) B. Horn, A.; Jessica Sully, K. ATR-IR Spectroscopic Studies of the Formation of Sulfuric Acid and Sulfuric Acid Monohydrate Films. *Physical Chemistry Chemical Physics* **1999**, *1* (16), 3801–3806. <https://doi.org/10.1039/A904544I>.



Data Availability Statement

View Article Online
DOI: 10.1039/D5FD00167F

The datasets supporting this article, titled "Structure-Controlled Sulfur Poisoning and Hydrogen-Induced Regeneration in Single Pd Nanoparticles Probed by Nanospectroscopy" are openly available on Zenodo and can be accessed via the DOI: 10.5281/zenodo.17934083.

